 doi:10.20944/preprints202009.0125.v1

Direct laser deposition metal 3D printing at different temperatures of the printer's chamber: computer simulation

Hamed Hosseinzadeh[1]

[1] *Henry M. Rowan College of Engineering, Rowan University, NJ*

[*] *Corresponding author: Email address: Hamed@uwalumni.com*

Abstract

Metal 3D printing technology is a promising manufacturing method. The quality of the printed product can pass for mechanical application, if the anisotropy of the microstructure, imperfections, deformation, and residual stress of the printed sample could be lower than the appropriate level or if they are fully illuminated. Thermal stress is one of the significant reasons for deformation in the 3D printed samples. Thermal stresses are the direct consequence of the local temperature gradient. In this research, the effect of the temperature printer's chamber (from room temperature to 900 C) was studied on thermal stress and subsequent total deformation in the printed sample. The printed sample is a six-layers-printed walk, which could be considered as a building block of other complex shapes and give us inside about deformation. The computational results show a meaningful reduction in thermal stress and deformation at the higher temperature of the printer's chamber. The lower final deformation of the printed sample is an important subject, especially for samples with complex shapes.

Keywords: Metal 3D printing, Thermal stress, Additive manufacturing, Mechanical properties, Thermomechanical simulation

- **Introduction**

Generally, the additive manufacturing process is using a heat source to deposit the melted materials layer by layer. 3D printing is a rapid prototyping, and metal 3D printing can be beneficial for producing non-structural applications for design purposes [1]. ASTM Standard F2792 has categorized additive manufacturing processes as Directed Energy Deposition (DED) and Powder Bed Fusion (PBF). Recently, metal 3D printing became more popular, and the microstructure/mechanical properties of the printed sample were experimentally studied [2–7]. Although there are some examples of 3D printed samples ready for application without additional postprocessing [8, 9], mechanical properties and microstructure of the metal 3d printed samples are not fully reliable for applications without postprocessing, especially for load-bearing applications. So, most printed samples need additional postprocessing [10, 11], and the effect of heat treatment on mechanical properties/microstructure needs to be studied in detail [12]. Thermal history during printing and melting/solidification conditions are controlling subsequent microstructure (then mechanical properties), thermal deformation, and thermal stress[13]. The simulation gives many details about thermal history during printing [7, 14–17], and the computational

Preprints (www.preprints.org) | NOT PEER-REVIEWED | Posted: 5 September 2020 doi:10.20944/preprints202009.0125.v1

results could be used for the optimization of the manufacturing process. There are some researches that coupled macroscale thermal simulation coupled with mesoscale microstructural evaluation [18–21]. There are several published kinds of research on mesoscale microstructural simulations for powder bed-based additive manufacturing in the first layer of the print [22–27]. In addition, there are researches on addressing the grain structure of the additively manufactured materials, especially for powder bed fusion [27–30]. There are some experimental and computational investigations and papers discussed on thermal stress and deformation in additively manufactured metallic alloys [1, 31–33]. Thermal stress and deformation of additively manufactured are about several hundred MPa [34, 35] and several micrometers for small samples [36–39], respectively. This level of deformation is high enough, especially for complex shapes to reject the printed sample for application. So, we need to investigate some methods to optimize and reduce the level of thermal stress and deformation.

Although parameters like scan speed, laser power, and metal powder feeding rate in the DLD method could vary the level of thermal stress and subsequent deformation, the temperature of the printer's chamber may have a considerable effect on thermal stress, which investigated in this research. This research computationally presented the effect of different temperatures of the printer's chamber on thermal stress and local deformation of the printed sample by the direct laser deposition (DLD) method.

- **Computational method**

In this research, AM Comp Tech computational package for process modeling metal 3D printing was used (http://manufacture.technology/). The computational outputs of this code are 3D thermal and mechanical (von Mises stress/deformation) history during metal 3D printing by the DLD printing method. The software is solving conservative equations (conservation of energy and momentum) by finite difference numerical methods. Fig 1 shows the computational algorithm of the simulation in this research.

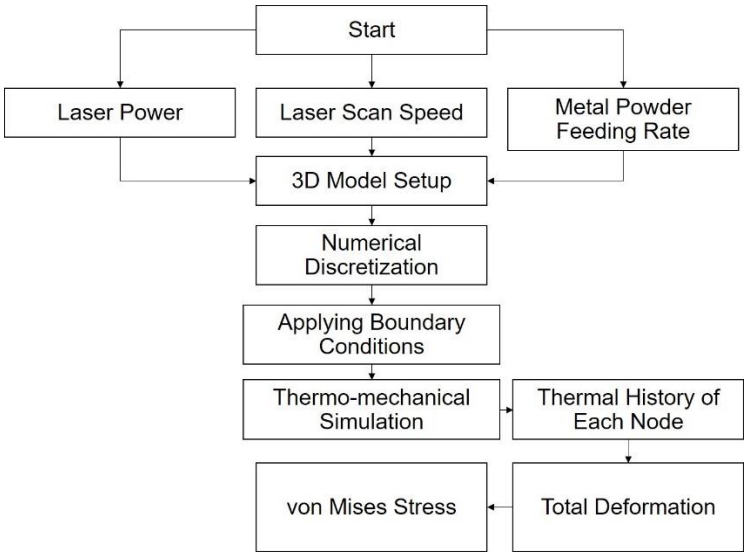

Fig 1 The computational algorithm of the simulation in this research. The computational outputs are total deformation and von Mises stress.

Preprints (www.preprints.org) | NOT PEER-REVIEWED | Posted: 5 September 2020 doi:10.20944/preprints202009.0125.v1

- Thermal analysis

Equation 1 was used for thermal analysis in which ρ is density, C_p is the specific heat, T is temperature, t is time, λ_i is the thermal conductivity, and Q is the source of heat. h represents both the thermal convection and radiation coefficients. The value of β was considered to be 0.9, as recommended for hot-rolled steels [40].

$$\rho C_p \frac{\partial T}{\partial t} = \nabla.(\lambda_i \nabla T) + Q \qquad (1)$$

$$-\nabla.(\lambda_i \nabla T) = h(T - T_\infty) \qquad (2)$$

$$h = 0.00241 \times \beta \times T^{1.61}$$

The energy balance in the equation (2) was applied as a thermal boundary condition. This equation has the physical meaning of thermal convection and radiation. In this simulation, the thermal conductivity and specific heat capacity are considered temperature-dependent (Fig 2).

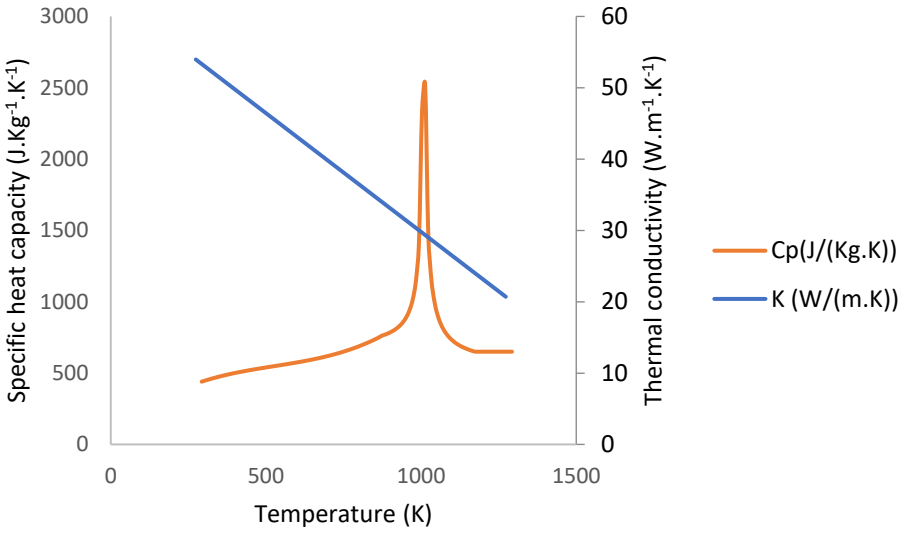

Fig 2 The temperature dependency of the thermal conductivity and specific heat capacity.

- Mechanical analysis

The equations 3 to 7 were used to calculate the displacement of each position as a result of temperature (thermomechanical simulation). Then, the results were used to calculate stress and strain. The used equations are as follows which ε is the strain, σ is stress, E is the module of elasticity, α is thermal expansion coefficient, υ is the Poisson ratio, λ and μ are Lame coefficients, u, v and w are displacement in x, y and z are directions, respectively:

Preprints (www.preprints.org) | NOT PEER-REVIEWED | Posted: 5 September 2020 doi:10.20944/preprints202009.0125.v1

$$\begin{cases} \varepsilon_{xx} = \dfrac{\partial u}{\partial x}; & \varepsilon_{xy} = \varepsilon_{yx} = \dfrac{1}{2}\left(\dfrac{\partial u}{\partial y} + \dfrac{\partial v}{\partial x}\right) \\ \varepsilon_{yy} = \dfrac{\partial v}{\partial y}; & \varepsilon_{yz} = \varepsilon_{yz} = \dfrac{1}{2}\left(\dfrac{\partial w}{\partial y} + \dfrac{\partial v}{\partial z}\right) \\ \varepsilon_{zz} = \dfrac{\partial w}{\partial z}; & \varepsilon_{zx} = \varepsilon_{xz} = \dfrac{1}{2}\left(\dfrac{\partial u}{\partial z} + \dfrac{\partial w}{\partial x}\right) \end{cases} \quad (3)$$

$$\begin{cases} \sigma_{xx} = 2\mu\varepsilon_{xx} + \lambda\left(\varepsilon_{xx} + \varepsilon_{yy} + \varepsilon_{zz}\right) - \dfrac{E\alpha T}{1-2\upsilon}; & \sigma_{zy} = \sigma_{yz} = 2\mu\varepsilon_{yz} \\ \sigma_{yy} = 2\mu\varepsilon_{yy} + \lambda\left(\varepsilon_{xx} + \varepsilon_{yy} + \varepsilon_{zz}\right) - \dfrac{E\alpha T}{1-2\upsilon}; & \sigma_{zx} = \sigma_{xz} = 2\mu\varepsilon_{zx} \\ \sigma_{zz} = 2\mu\varepsilon_{zz} + \lambda\left(\varepsilon_{xx} + \varepsilon_{yy} + \varepsilon_{zz}\right) - \dfrac{E\alpha T}{1-2\upsilon}; & \sigma_{xy} = \sigma_{yx} = 2\mu\varepsilon_{xy} \end{cases} \quad (4)$$

$$\mu = \frac{E}{2(1+\upsilon)}; \quad \lambda = \frac{E\upsilon}{(1+\upsilon)(1-2\upsilon)} \quad (5)$$

Equation 5 is the force equilibrium equation, and we could extract equation 6 by combining equations 2 to 5 to calculate displacement induced by temperature gradient.

$$\begin{cases} \dfrac{\partial \sigma_{xx}}{\partial x} + \dfrac{\partial \sigma_{yx}}{\partial y} + \dfrac{\partial \sigma_{zx}}{\partial z} = 0 \\ \dfrac{\partial \sigma_{xy}}{\partial x} + \dfrac{\partial \sigma_{yy}}{\partial y} + \dfrac{\partial \sigma_{zy}}{\partial z} = 0 \\ \dfrac{\partial \sigma_{xz}}{\partial x} + \dfrac{\partial \sigma_{yz}}{\partial y} + \dfrac{\partial \sigma_{zz}}{\partial z} = 0 \end{cases} \quad (6)$$

$$\begin{cases} \mu\left(\dfrac{\partial^2 u}{\partial x^2} + \dfrac{\partial^2 u}{\partial y^2} + \dfrac{\partial^2 u}{\partial z^2}\right) + (\mu+\lambda)\left(\dfrac{\partial^2 u}{\partial x^2} + \dfrac{\partial^2 v}{\partial y \partial x} + \dfrac{\partial^2 w}{\partial z \partial x}\right) - \dfrac{E\alpha}{1-2\upsilon}\dfrac{\partial T}{\partial x} = 0 \\ \mu\left(\dfrac{\partial^2 v}{\partial x^2} + \dfrac{\partial^2 v}{\partial y^2} + \dfrac{\partial^2 v}{\partial z^2}\right) + (\mu+\lambda)\left(\dfrac{\partial^2 u}{\partial y \partial x} + \dfrac{\partial^2 v}{\partial y^2} + \dfrac{\partial^2 w}{\partial z \partial y}\right) - \dfrac{E\alpha}{1-2\upsilon}\dfrac{\partial T}{\partial y} = 0 \\ \mu\left(\dfrac{\partial^2 w}{\partial x^2} + \dfrac{\partial^2 w}{\partial y^2} + \dfrac{\partial^2 w}{\partial z^2}\right) + (\mu+\lambda)\left(\dfrac{\partial^2 u}{\partial z \partial x} + \dfrac{\partial^2 v}{\partial z \partial y} + \dfrac{\partial^2 w}{\partial z^2}\right) - \dfrac{E\alpha}{1-2\upsilon}\dfrac{\partial T}{\partial z} = 0 \end{cases} \quad (7)$$

Equation 1 and 7 were simultaneously solved by the finite difference method.

The value of modulus of elasticity is temperature-dependent, and fig 3 shows the used temperature dependency of modulus of elasticity in this research.

Preprints (www.preprints.org) | NOT PEER-REVIEWED | Posted: 5 September 2020 doi:10.20944/preprints202009.0125.v1

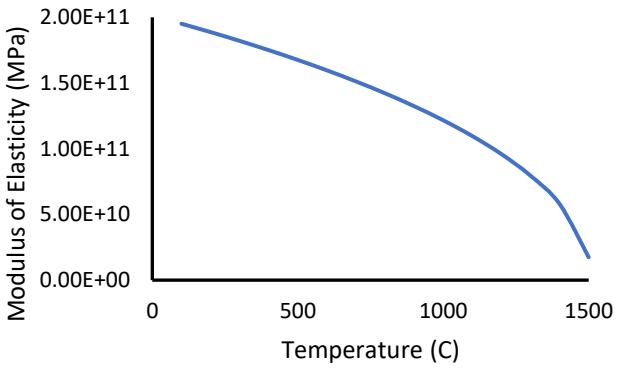

Fig 3 Dependency of modulus of elasticity on temperature.

- Powder feeding

In metal 3D printing and DLD method, metal powders are blown to the laser to be melted by laser and thus, adding a new layer during metal 3D printing. A method was used to consider this subject in the simulation. New nodes (for newly melted powders which are added from the nozzle) will be added to the defined position (exactly under the nozzle) on the previously printed part of the model during each time step. This is the used method to update the model to consider newly melted metal powders through the nozzle (fig 4).

Preprints (www.preprints.org) | NOT PEER-REVIEWED | Posted: 5 September 2020 doi:10.20944/preprints202009.0125.v1

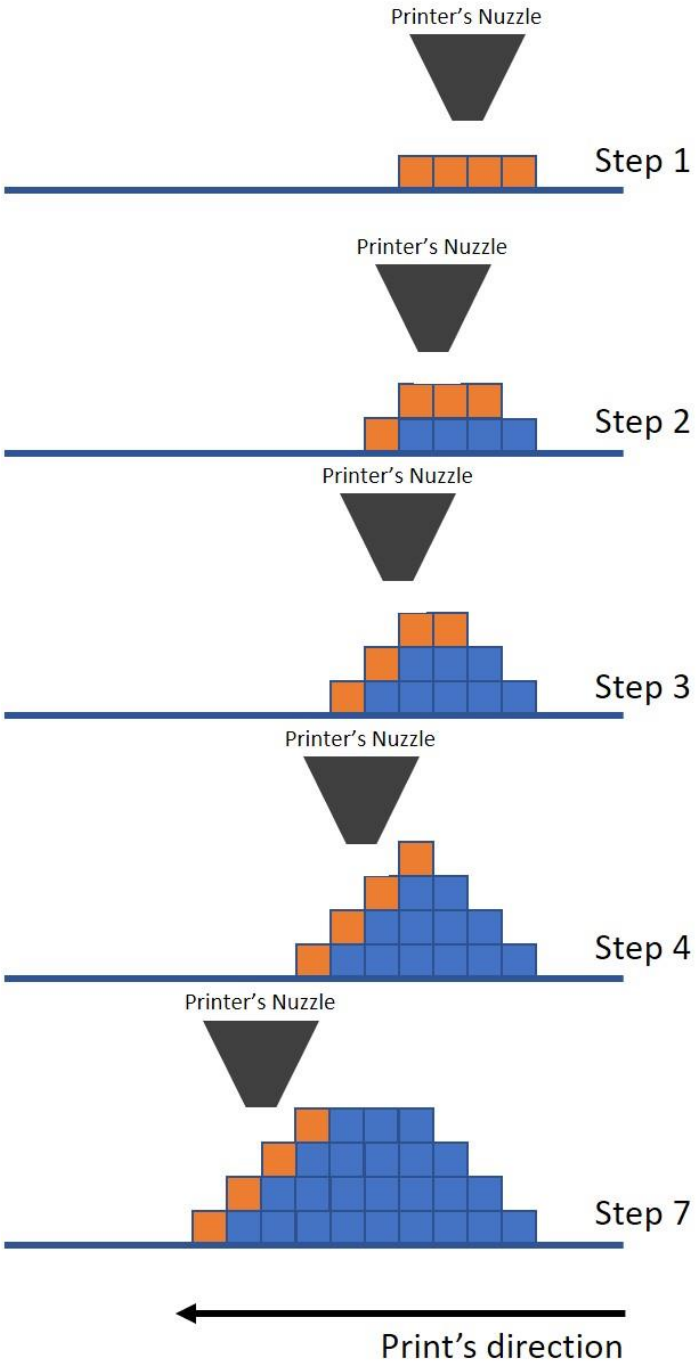

Fig 4 Schematic shows how recently melted metal powders will be added to the model during each time step of simulation to construct layers on each other.

In this research, we considered a constant temperature for melted powders as the initial condition rather than using laser energy and conventional Gaussian surface heat source, top-hat distribution, or

Preprints (www.preprints.org) | NOT PEER-REVIEWED | Posted: 5 September 2020 doi:10.20944/preprints202009.0125.v1

Goldak's double ellipsoid heat source [41] as a boundary condition. The higher temperature of melted powders means higher laser power.

- **Results and discussions**

In this research, a wall is printed to check the thermomechanical responses if the sample prints at different temperatures of the printer's chamber. This wall could be considered as a building block for any other complex shapes. The printed wall has 2.5 mm width, 20 mm length, and 6 mm height. The beam (travel) speed and powder feeding rate are set to 2 $mm.s^{-1}$, 100 $mg.s^{-1}$, respectively. Each printed pass has a 1 mm height with these travel speed and powder feeding rates. So, this wall must be printed with six passes. Fig 5 shows how the printed layers are constructed during the simulation. The final printed wall has also shown in fig 5 b, and a cross-section was selected to check the simulation results. This cross-section is in the middle of the printed wall.

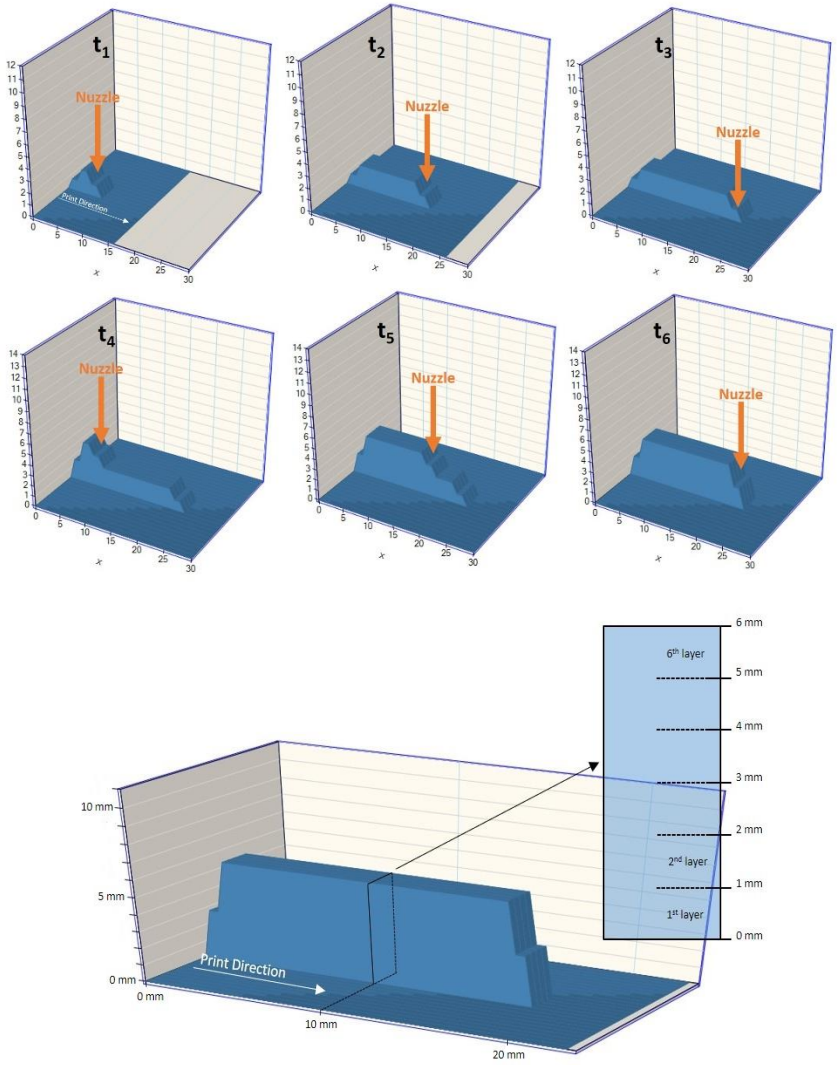

Fig 5 a) The print stage in the simulation at different time steps (t_1>t_2> t_3>t_4> t_5>t_6), and b) Printed sample built with six layers and the cross-section shows the layers which has 1 mm height each.

Preprints (www.preprints.org) | NOT PEER-REVIEWED | Posted: 5 September 2020 doi:10.20944/preprints202009.0125.v1

This wall was printed at different temperatures of the chamber. The simulated results of heating and cooling curves for 27 C, 100C, 200 C, 300 C, 400 C, 500 C, 600 C, 700 C, 800 C, and 900 C temperature of the chamber at some points were shown in fig 6.

Thermal stress and deformation are the direct consequence of the thermal history of the printed sample, and they would have a lower value if the local temperature gradient is lower. The local temperature gradient is lower in the samples, which are printed at the higher chamber's temperature. Hence, it could be expected to lower thermal stress if the sample is printed at a higher temperature. This subject is shown in fig 7, and the von Mises stress shows a considerable reduction in stress level by 3D printing at a higher temperature of the printer's chamber. Although the lower thermal stress may cause lower deformation, the modulus of elasticity has a much lower value at high temperatures. It means that the printed sample is softer at a higher temperature. So, the total deformation must be checked to see if it would be reduced by increasing the temperature of the printer's chamber or not.

Simulation results show a meaningful reduction in the total deformation if the sample is printed at a higher temperature. This subject has been shown in fig 8. The total deformation is the vector sum of all directional displacements of the systems. The computational results show that the total deformation is in the range of micrometers.

Preprints (www.preprints.org) | NOT PEER-REVIEWED | Posted: 5 September 2020 doi:10.20944/preprints202009.0125.v1

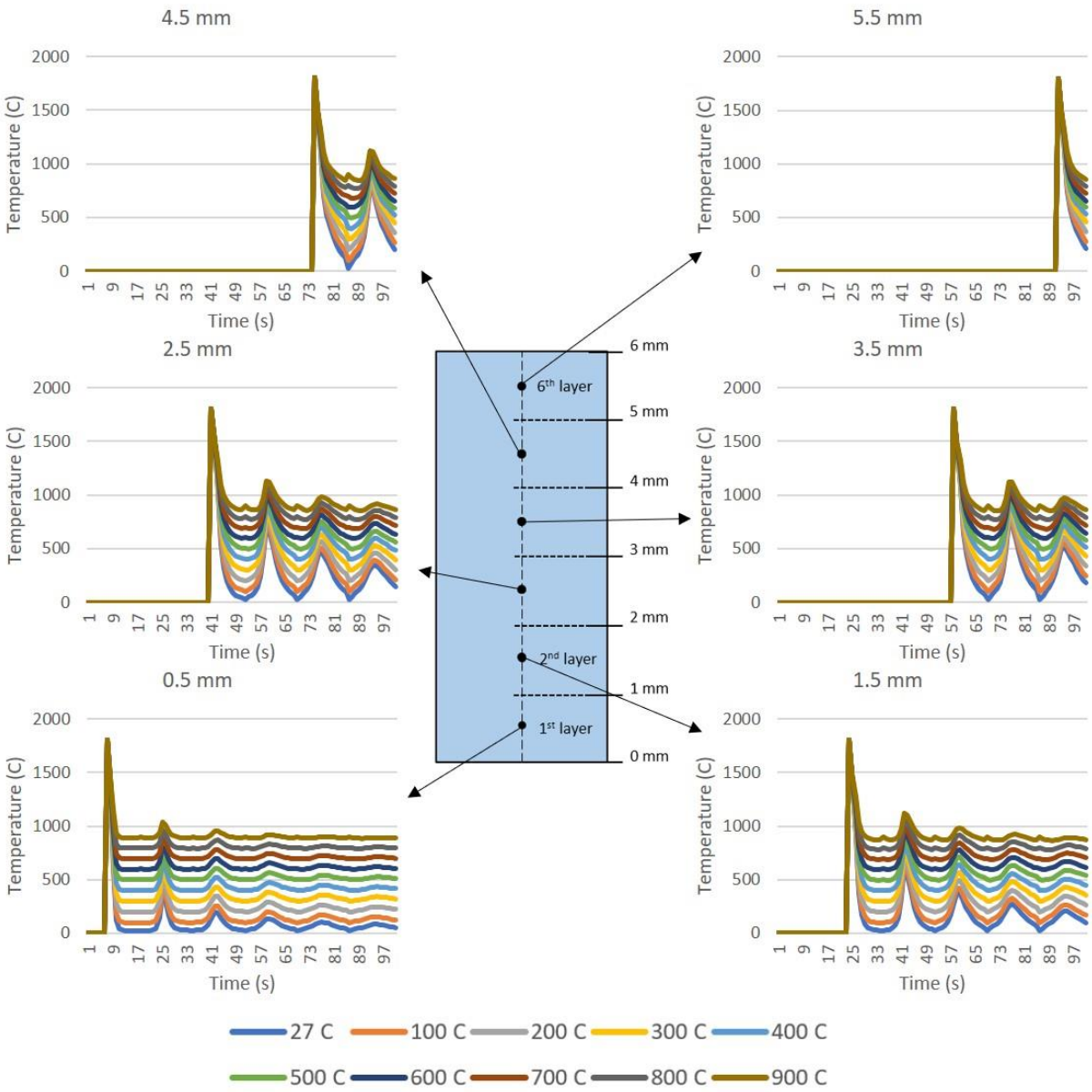

Fig 6 Simulated temperature profiles at different positions and temperatures of the printer's chamber.

Preprints (www.preprints.org) | NOT PEER-REVIEWED | Posted: 5 September 2020 doi:10.20944/preprints202009.0125.v1

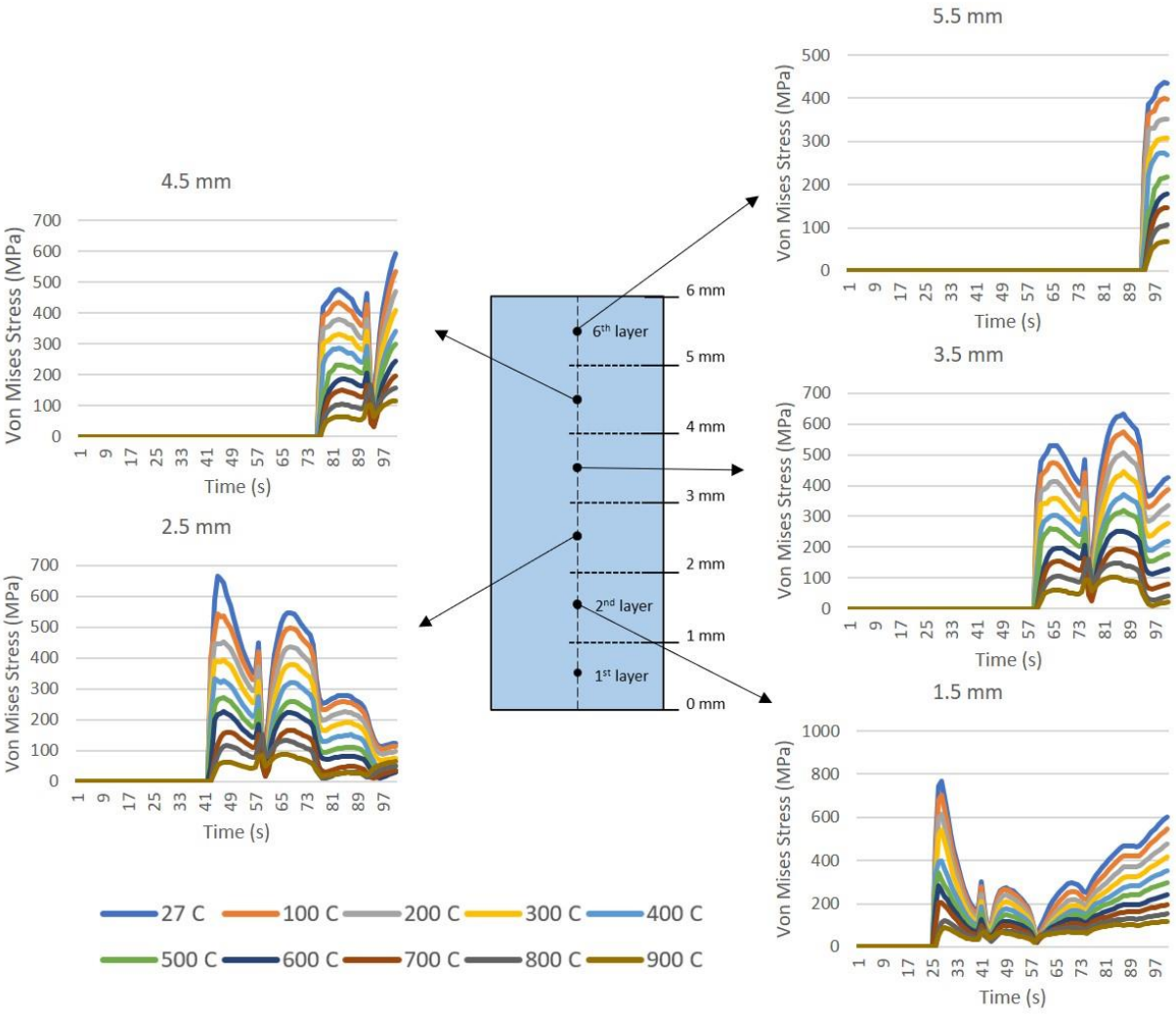

Fig 7 Simulated von Mises stress at different positions and temperatures of the printer's chamber.

Preprints (www.preprints.org) | NOT PEER-REVIEWED | Posted: 5 September 2020 doi:10.20944/preprints202009.0125.v1

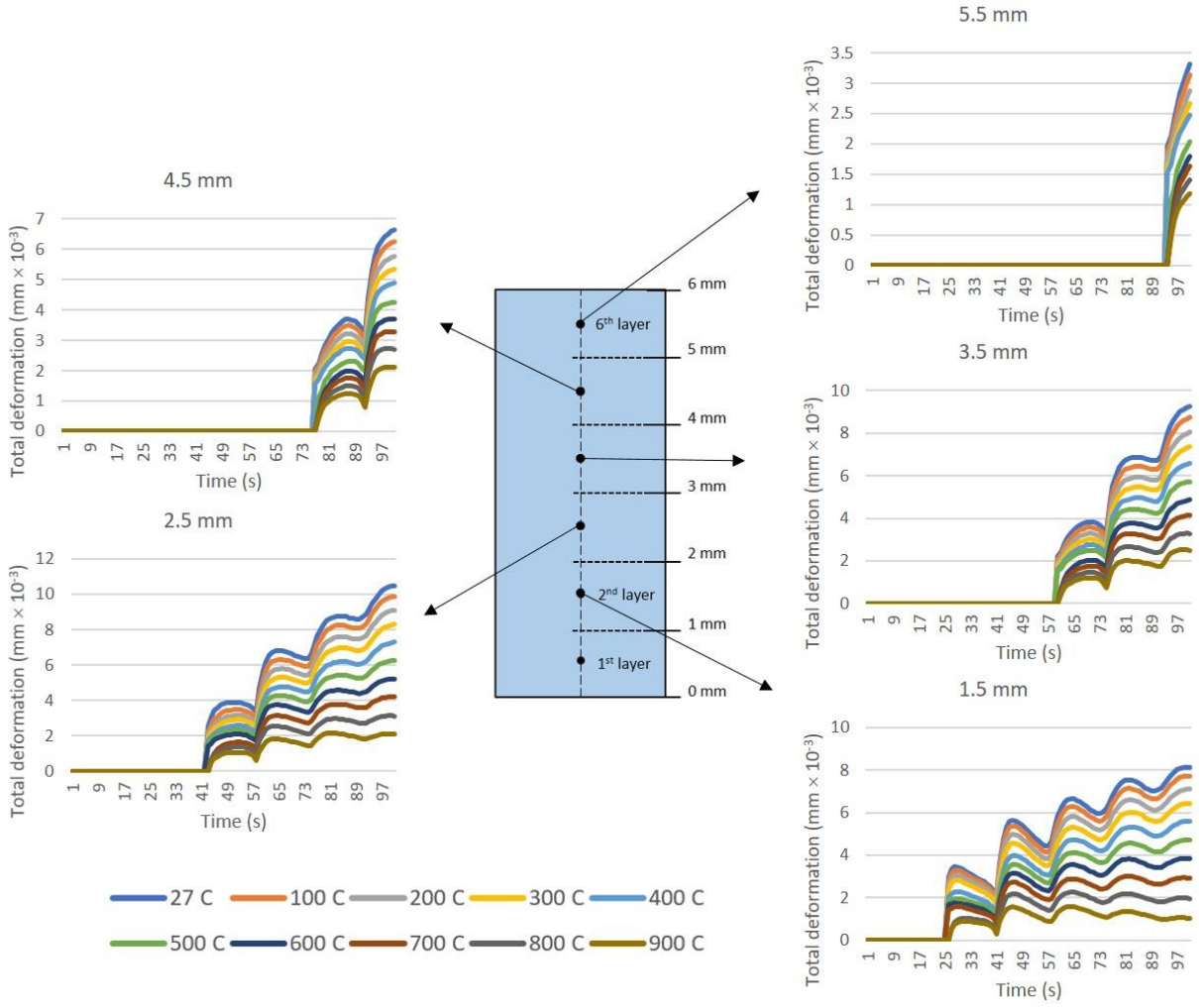

Fig 8 Simulated total deformation at different positions and temperatures of the printer's chamber.

So far, the thermal stress and total deformation have been checked at some key points of the printed sample to see how the values changes by the time.

The thermal stress and deformation levels in the printed sample could be shown for some cross-sections. This subject was checked at three cross-sections exactly at the end of the printing. The temperature, thermal stress, and total deformation profiles at the end of the printing were shown in fig 9, fig 10, and fig 11, respectively. The simulation results confirm a lower level of thermal stress and total deformation if the sample is printed at a higher temperature.

As it is obvious in fig 9, the temperature gradient through the printed sample is lower at a higher temperature. A higher temperature gradient means higher thermal stress and deformation if the modulus of elasticity remains constant. Fig 3 shows a strong dependency of modulus of elasticity with temperature.

Preprints (www.preprints.org) | NOT PEER-REVIEWED | Posted: 5 September 2020 doi:10.20944/preprints202009.0125.v1

So, the combination of the value of elastic modulus and local temperature gradient shapes the level of thermal stress and the total deformation. For example, if the sample prints at 27 C (chamber's temperature), the temperature gradient is lower for the cross-sections closer to the substrate. Fig 9 b shows that the temperature gradient is lower for at 1.5 mm cross-section in comparison with 3.5 mm and then 5.5 mm, which 5.5 mm has a higher temperature gradient, which shows an increase in the thermal stress in fig 10.

If it is technically possible to print at a higher temperature, the total deformation level is considerably lower versus printing at room temperature. If the sample experiences higher temperatures especially higher than austenitization temperature of steel alloys, the final microstructure would be almost uniform and possibly no columnar grain structure.

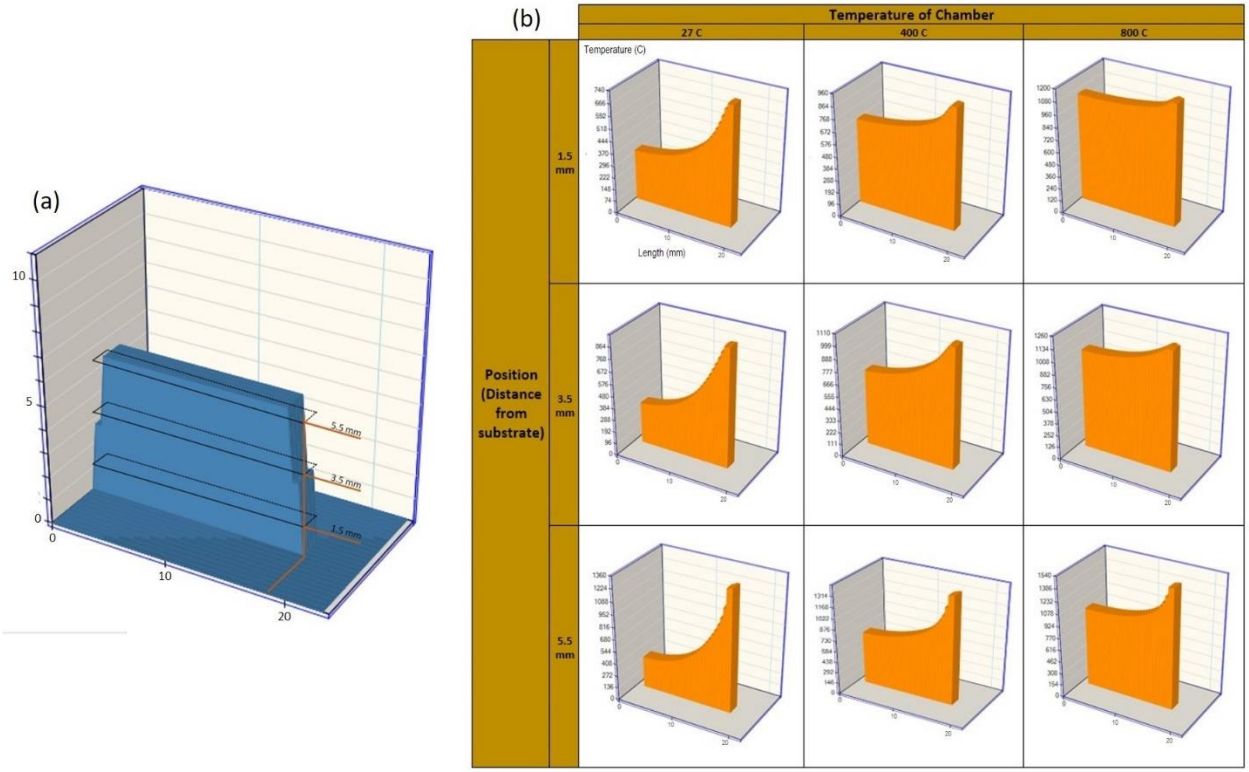

Fig 9 The temperature profiles at the end of the print for the chamber's temperature of 27C, 400C, and 800C.

Preprints (www.preprints.org) | NOT PEER-REVIEWED | Posted: 5 September 2020 doi:10.20944/preprints202009.0125.v1

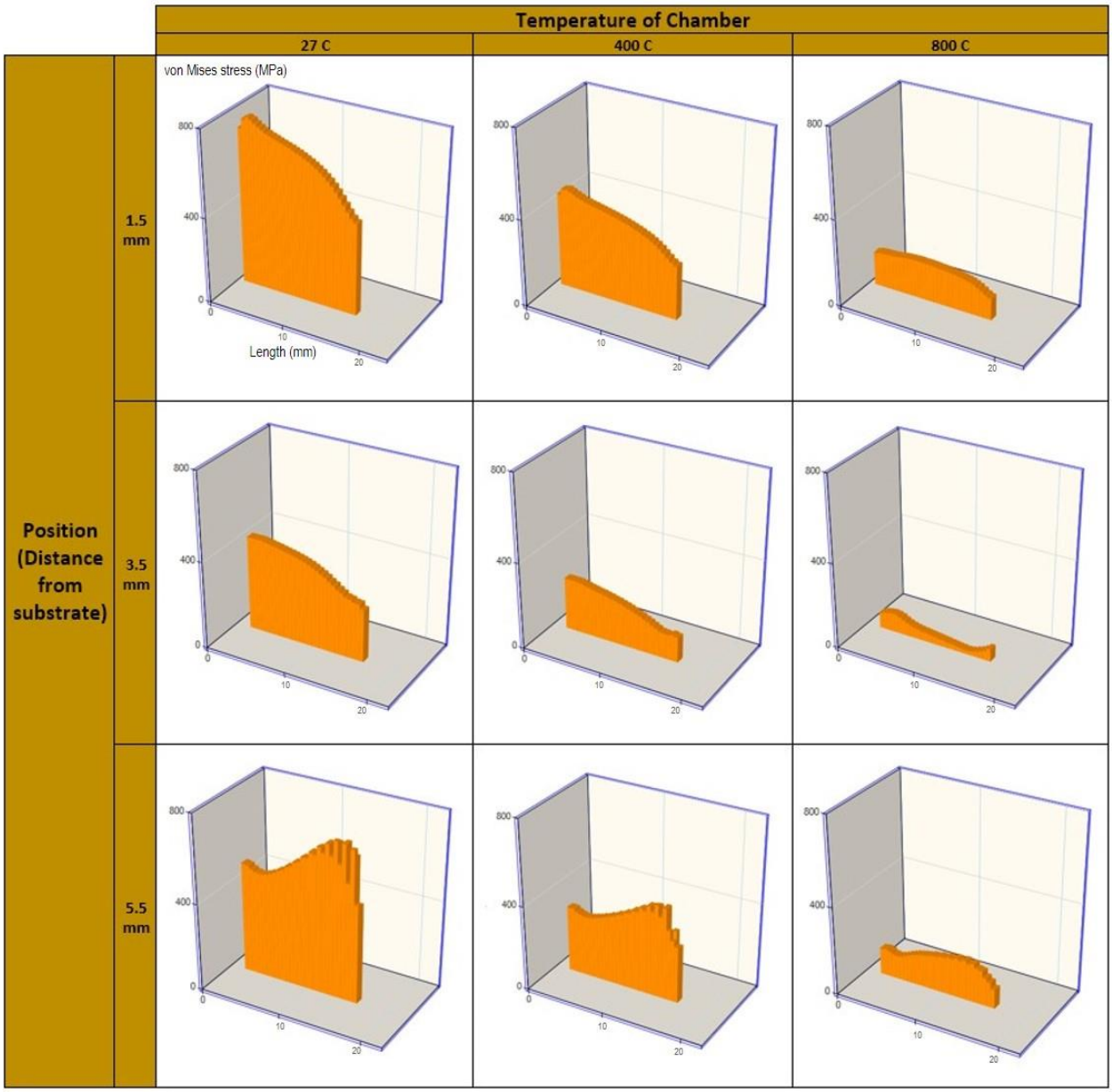

Fig 10 The von Mises stress profiles at the end of the print for the chamber's temperature of 27C, 400C, and 800C.

Preprints (www.preprints.org) | NOT PEER-REVIEWED | Posted: 5 September 2020 doi:10.20944/preprints202009.0125.v1

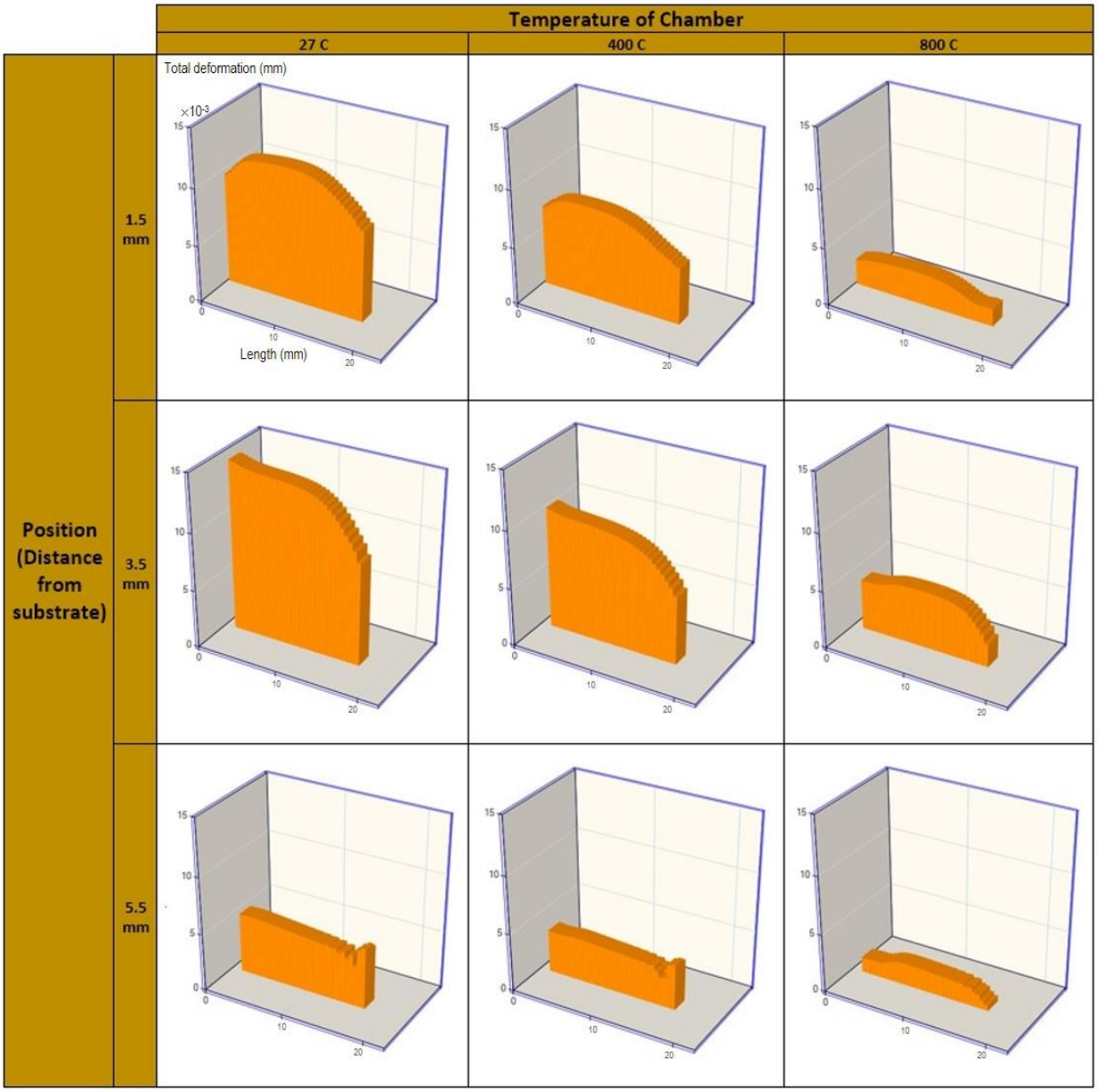

Fig 11 The total deformation profiles at the end of the print for the chamber's temperature of 27C, 400C, and 800C.

- **Conclusions**

Metal 3D printing is an exciting manufacturing method but needs more optimizations of the printing process to have a reliable product directly for structural applications. This research tried to address the effect of the temperature of the printer's chamber on the evolution of the thermal stress and total deformation in the 3D printed sample by the DLD method. The simulation was done at constant print speed, laser power, and rate of metal powders injection but the different temperature of the printer's chamber. Simulation results show that the temperature of the printer's chamber influences the

thermomechanical response. The thermal stress in the 3D printed sample by the DLD method is reducing by increasing the temperature of the printer's chamber. The total deformation in the 3D printed sample by the DLD method is reducing by increasing the temperature of the printer's chamber. If it is technically possible to print at a higher temperature, the total deformation level is considerably lower versus printing at room temperature.

References

1. Debroy T, Wei HL, Zuback JS, et al (2018) Progress in Materials Science Additive manufacturing of metallic components – Process , structure and properties. 92:112–224
2. Sergio M, Lima F De, Sankaré S (2014) Microstructure and mechanical behavior of laser additive manufactured AISI 316 stainless steel stringers microstructure and mechanical behavior of laser additive manufactured AISI 316 stainless steel stringers. J Mater 55:526–532. https://doi.org/10.1016/j.matdes.2013.10.016
3. Shi X, Ma S, Liu C, et al (2017) Materials Science & Engineering A Selective laser melting-wire arc additive manufacturing hybrid fabrication of Ti-6Al-4V alloy : Microstructure and mechanical properties. Mater Sci Eng A 684:196–204. https://doi.org/10.1016/j.msea.2016.12.065
4. Pham MS, Dovgyy B, Hooper PA (2017) Materials Science & Engineering A Twinning induced plasticity in austenitic stainless steel 316L made by additive manufacturing. Mater Sci Eng A 704:102–111. https://doi.org/10.1016/j.msea.2017.07.082
5. Croteau JR, Grif S, Rossell MD, et al (2018) Acta Materialia Microstructure and mechanical properties of Al-Mg-Zr alloys processed by selective laser melting. 153:35–44. https://doi.org/10.1016/j.actamat.2018.04.053
6. Nassar AR, Reutzel EW (2015) Additive Manufacturing of Ti-6Al-4V Using a Pulsed Laser Beam. Metall Mater Trans A 46A:2781–2789. https://doi.org/10.1007/s11661-015-2838-z
7. Shamsaei N, Yadollahi A, Bian L, Thompson SM (2015) An overview of Direct Laser Deposition for additive manufacturing; Part II: Mechanical behavior, process parameter optimization and control. Addit Manuf 8:12–35. https://doi.org/10.1016/j.addma.2015.07.002
8. Shayesteh Moghaddam N, Saedi S, Amerinatanzi A, et al (2019) Achieving superelasticity in additively manufactured NiTi in compression without post-process heat treatment. Sci Rep 9:1–11. https://doi.org/10.1038/s41598-018-36641-4
9. Wang YM, Voisin T, McKeown JT, et al (2018) Additively manufactured hierarchical stainless steels with high strength and ductility. Nat Mater 17:63–70. https://doi.org/10.1038/NMAT5021
10. Li J, Cheng X, Li Z, et al (2018) Materials Science & Engineering A Improving the mechanical properties of Al-5Si-1Cu-Mg aluminum alloy produced by laser additive manufacturing with post-process heat treatments. Mater Sci Eng A 735:408–417. https://doi.org/10.1016/j.msea.2018.08.074
11. Zhuo L, Wang Z, Zhang H, et al (2019) Effect of post-process heat treatment on microstructure and properties of selective laser melted AlSi10Mg alloy. Mater Lett 234:196–200.

https://doi.org/10.1016/j.matlet.2018.09.109

12. Yadollahi A, Shamsaei N, Thompson SM, Seely DW (2015) Effects of process time interval and heat treatment on the mechanical and microstructural properties of direct laser deposited 316L stainless steel. Mater Sci Eng A 644:171–183. https://doi.org/10.1016/j.msea.2015.07.056

13. Cunningham CR, Flynn JM, Shokrani A, et al (2018) Invited review article : Strategies and processes for high quality wire arc additive manufacturing. Addit Manuf 22:672–686. https://doi.org/10.1016/j.addma.2018.06.020

14. Steuben JC, Birnbaum AJ, Michopoulos JG, Iliopoulos AP (2019) Enriched analytical solutions for additive manufacturing modeling and simulation. Addit Manuf 25:437–447. https://doi.org/10.1016/j.addma.2018.10.017

15. Peng H, Ghasri-khouzani M, Gong S, et al (2018) Fast prediction of thermal distortion in metal powder bed fusion additive manufacturing : Part 1 , a thermal circuit network model. Addit Manuf 22:852–868. https://doi.org/10.1016/j.addma.2018.05.023

16. Mcmillan M, Leary M, Brandt M (2017) Computationally efficient finite difference method for metal additive manufacturing : A reduced-order DFAM tool applied to SLM. Mater Des 132:226–243. https://doi.org/10.1016/j.matdes.2017.06.058

17. Cheng L, Yang Q, Zhang P, et al (2016) Finite element modeling and validation of thermomechanical behavior of Ti- 6Al-4V in directed energy deposition additive manufacturing Finite element modeling and validation of thermomechanical behavior of Ti-6Al-4V in directed energy deposition additive . Addit Manuf 12:169–177. https://doi.org/10.1016/j.addma.2016.06.012

18. Panwisawas C, Sovani Y, Anderson MJ, et al (2016) A Multi-Scale Multi-Physics Approach to Modelling of Additive Manufacturing in Nickel-Based Superalloys. Superalloys2016 Warrendale, TMS 1021–1030. https://doi.org/10.1002/9781119075646.ch108

19. Methods C, Mech A, Yan W, et al (2018) An integrated process – structure – property modeling framework for additive manufacturing. Comput Methods Appl Mech Engrg 339:184–204. https://doi.org/10.1016/j.cma.2018.05.004

20. Zhang Z, Tan ZJ, Yao XX, et al (2018) Numerical methods for microstructural evolutions in laser additive manufacturing. https://doi.org/10.1016/j.camwa.2018.07.011

21. Michopoulos JG, Iliopoulos AP, Steuben JC, et al (2018) On the multiphysics modeling challenges for metal additive manufacturing processes. Addit Manuf 22:784–799. https://doi.org/10.1016/j.addma.2018.06.019

22. Zinovieva O, Zinoviev A, Ploshikhin V (2018) Three-dimensional modeling of the microstructure evolution during metal additive manufacturing. Comput Mater Sci 141:207–220. https://doi.org/10.1016/j.commatsci.2017.09.018

23. Rai A, Helmer H, Körner C (2017) Simulation of grain structure evolution during powder bed based additive manufacturing. Addit Manuf 13:124–134. https://doi.org/10.1016/j.addma.2016.10.007

24. Rodgers TM, Madison JD, Tikare V (2017) Simulation of metal additive manufacturing microstructures using kinetic Monte Carlo. Comput Mater Sci 135:78–89.

https://doi.org/10.1016/j.commatsci.2017.03.053

25. Lu L, Sridhar N, Zhang Y (2018) Acta Materialia Phase fi eld simulation of powder bed-based additive manufacturing. Acta Mater 144:801–809. https://doi.org/10.1016/j.actamat.2017.11.033

26. Sahoo S, Chou K (2016) Phase-field simulation of microstructure evolution of Ti-6Al-4V in electron beam additive manufacturing process. Addit Manuf 9:14–24. https://doi.org/10.1016/j.addma.2015.12.005

27. Liu PW, Ji YZ, Wang Z, et al (2018) Investigation on evolution mechanisms of site-specific grain structures during metal additive manufacturing. J Mater Process Technol 257:191–202. https://doi.org/10.1016/j.jmatprotec.2018.02.042

28. Yan F, Xiong W, Faierson EJ (2017) Grain Structure Control of Additively Manufactured. 1–11. https://doi.org/10.3390/ma10111260

29. Markl M, Körner C (2016) Multiscale Modeling of Powder Bed–Based Additive Manufacturing. Annu Rev Mater Res 46:93–123. https://doi.org/10.1146/annurev-matsci-070115-032158

30. Koepf JA, Gotterbarm MR, Markl M, Körner C (2018) 3D multi-layer grain structure simulation of powder bed fusion additive manufacturing. Acta Mater 152:119–126. https://doi.org/10.1016/j.actamat.2018.04.030

31. Wu AS, Brown DW, Kumar M, et al (2014) An Experimental Investigation into Additive Manufacturing-Induced Residual Stresses in 316L Stainless Steel. Metall Mater Trans A Phys Metall Mater Sci 45:6260–6270. https://doi.org/10.1007/s11661-014-2549-x

32. Zaeh MF, Branner G (2010) Investigations on residual stresses and deformations in selective laser melting. Prod Eng 4:35–45. https://doi.org/10.1007/s11740-009-0192-y

33. Moat RJ, Pinkerton AJ, Li L, et al (2011) Residual stresses in laser direct metal deposited Waspaloy. Mater Sci Eng A 528:2288–2298. https://doi.org/10.1016/j.msea.2010.12.010

34. Johnson KL, Rodgers TM, Underwood OD, et al (2018) Simulation and experimental comparison of the thermo-mechanical history and 3D microstructure evolution of 304L stainless steel tubes manufactured using LENS. Comput Mech 61:559–574. https://doi.org/10.1007/s00466-017-1516-y

35. Peng H, Ghasri-Khouzani M, Gong S, et al (2018) Fast prediction of thermal distortion in metal powder bed fusion additive manufacturing: Part 2, a quasi-static thermo-mechanical model. Addit Manuf 22:869–882. https://doi.org/10.1016/j.addma.2018.05.001

36. Santos LS, Gupta SK, Bruck HA (2018) Simulation of buckling of internal features during selective laser sintering of metals. Addit Manuf 23:235–245. https://doi.org/10.1016/j.addma.2018.08.002

37. Mayer T, Brändle G, Schönenberger A, Eberlein R (2020) Simulation and validation of residual deformations in additive manufacturing of metal parts. Heliyon 6:. https://doi.org/10.1016/j.heliyon.2020.e03987

38. Megahed M, Mindt HW, N'Dri N, et al (2016) Metal additive-manufacturing process and residual stress modeling. Integrating Materials and Manufacturing Innovation

39. Stender ME, Beghini LL, Sugar JD, et al (2018) A thermal-mechanical finite element workflow for

directed energy deposition additive manufacturing process modeling. Addit Manuf 21:556–566. https://doi.org/10.1016/j.addma.2018.04.012

40. Haddad-Sabzevar M, Haerian A, Seied-Hossein-Zadeh H (2009) A stochastic model for austenite phase formation during arc welding of a low alloy steel. J Mater Process Technol. https://doi.org/10.1016/j.jmatprotec.2008.08.039

41. Yan Z, Liu W, Tang Z, et al (2018) Review on thermal analysis in laser-based additive manufacturing. Opt Laser Technol 106:427–441. https://doi.org/10.1016/j.optlastec.2018.04.034